INSTITUTE OF PHYSICS PUBLISHING JOURNAL OF PHYSICS: CONDENSED MATTER

J. Phys.: Condens. Matter **16** (2004) S4619–S4638 PII: S0953-8984(04)84619-8

Zero-field muon spin relaxation studies of frustrated magnets: physics and analysis issues

D H Ryan[1], **J van Lierop**[2] **and J M Cadogan**[3]

[1] Center for the Physics of Materials, Physics Department, McGill University, 3600 University Street, Montreal, QC, H3A 2T8, Canada
[2] Department of Physics and Astronomy, University of Manitoba, Winnipeg, Manitoba, R3T 2N2, Canada
[3] School of Physics, The University of New South Wales, Sydney, NSW 2052, Australia

Received 19 January 2004
Published 24 September 2004
Online at stacks.iop.org/JPhysCM/16/S4619
doi:10.1088/0953-8984/16/40/012

Abstract

The exquisite sensitivity of zero-field muon spin relaxation to both static magnetic order and dynamic fluctuations has been used to study the ordering processes in a variety of exchange frustrated magnetic materials. Two distinct ordering events are identified, and they each clearly show both dynamic and static signatures. Phase diagrams for two classes of frustration are presented. We also provide an extensive discussion of both approximate and complete solutions to dynamic fitting functions, and show that the correct functions used in our analysis yield more accurate fits and quantitative agreement with independent measurements on the same samples.

1. Introduction

Frustration arises in magnetic systems through the presence of competing exchange interactions. If this frustration is randomly distributed, and is present at a sufficient density, then long-ranged magnetic order is not possible and the system becomes a spin glass. Assuming, as is the case for most real systems, that nearest-neighbour exchange interactions are dominant, we can distinguish two classes of exchange frustration: (1) *bond frustration*, where individual exchange bonds may be of either sign; and (2) *site frustration*, where all of the exchange bonds from an impurity site are opposite to those of the matrix. In both classes, the level of frustration is a tunable quantity, so the evolution in behaviour can be studied as the exchange distribution changes from all ferromagnetic (FM) to all antiferromagnetic (AF). The gross phenomenologies are similar in the two cases. Introducing AF bonds (or sites) leads to a reduction of the ferromagnetic ordering temperature (T_c) and the appearance of a new, lower transition temperature (T_{xy}) where spin components order perpendicular to the ferromagnetic order established at T_c. Beyond a critical concentration of frustration, x_c, there is a loss of all long-ranged order and the development of a spin glass.

The behaviour around T_c and the effects of increasing exchange frustration are readily studied by conventional magnetization and susceptibility methods, while confirmation that long-range ferromagnetic order is indeed established at T_c, and is not lost on further cooling (there is no 're-entrance') comes from neutron depolarization [1]. However, studying the region around T_{xy} is more challenging. Transverse ordering occurs in the presence of pre-existing ferromagnetic order, so the bulk response is dominated by the (largely technical) behaviour of the ferromagnet and its domain system. Mössbauer spectroscopy, especially with an applied external field, has been used to demonstrate that ordering perpendicular to the ferromagnetic axis does occur on cooling through T_{xy} [2–4]. Furthermore, the local spin correlations that develop below T_{xy} depend on whether bond [5, 6] or site [7] frustration is present. Unfortunately, the magnetic field used in the Mössbauer work has been shown to severely affect the behaviour at T_{xy}, with only a few teslas needed to almost fully suppress the transition [8].

Numerical simulations of bond [9] and site [10–12] frustrated model systems have led to the identification of a T_{xy}-signature that is accessible in zero applied field. In both cases, the ordering of the transverse spin components at T_{xy} is associated with a peak in the spin fluctuation rate. Ordinarily, such a peak would be detectable using bulk susceptibility; however, the overwhelming response of the pre-existing ferromagnetic order makes this impossible. We have turned therefore to zero-field muon spin relaxation (ZF-μSR) which is simultaneously sensitive both to static magnetic order *and* to fluctuations in that order, even in highly disordered materials. The ZF-μSR technique provides a complete and unambiguous separation of the static and dynamic influences on the relaxation signal, so one can be studied in the presence of the other: a critical requirement around T_{xy}.

The organization of the remainder of this review is as follows. Following a brief description of the samples and ZF-μSR methodology, we present results obtained for both bond and site frustrated systems. Analysis procedures are treated only briefly, with a severe caveat on validity, so that we can concentrate on the gross features of the signals and the phase diagrams derived from the ZF-μSR data. With the frustration effects on magnetic ordering established, we then turn to a more detailed discussion of muon relaxation functions, identifying the limitations of some popular approximations and showing that a full solution is possible, obviating the need for the more poorly motivated approximations, and yielding more accurate values for the derived parameters.

2. Experimental methods

Two bond frustrated alloy systems have been studied. a-Fe_xZr_{100-x} has the virtue of being a binary metallic glass with only a single magnetic species. It is stable for $88 \leqslant x \leqslant 93.2$ and evolves from a ferromagnet to a spin glass with increasing x [3, 13]. However, the spin glass regime is only barely accessible, as the critical concentration (x_c) is $\sim$92.8 [14]. In order to access the ferromagnet to spin glass crossover more clearly, we turned to a ruthenium-doped Fe–Zr glass: a-$Fe_{90-x}Ru_xZr_{10}$, where x_c is 2.3 [1, 15, 16]. While we have only studied this system as far as $x = 6$, the glass is stable at least as far as $x = 20$ [17], well into the spin glass regime. The effects of site frustration were investigated using a manganese-doped iron–metalloid glass: a-$(Fe_{1-x}Mn_x)_{78}Si_8B_{14}$ [7, 18], where $x_c = 0.31$ and the glass can be prepared at least up to $x = 0.5$.

Samples were prepared by arc-melting appropriate amounts of the pure elements under Ti-gettered argon, followed by melt-spinning with a tangential wheel speed of 55 m s^{-1} in pure helium. ZF-μSR measurements were made on the M13 and M20 beamlines at TRIUMF. Sample temperature was controlled between 5 and 300 K in a conventional He-flow cryostat.

Field-zero was set to better than 1 μT using a flux-gate magnetometer. Samples were 170–200 mg cm^{-2} thick over a 16 mm diameter active area. A pure silver (99.99%) mask prevented stray muons from striking any of the mounting hardware. Essentially 100% spin polarized μ^+ were implanted with their moments directed in the backward direction (i.e. along $-z$). The subsequent decay e^+ is emitted preferentially along the moment direction. The time dependence of the μ^+ polarization is conventionally followed by plotting the asymmetry (A) between scintillation detectors placed in the forward (F) and backward (B) directions relative to the initial μ^+ flight direction (A = (B − F)/(B + F)) as a function of time. Histograms containing $\sim 4 \times 10^7$ events were acquired with a timing resolution of 0.781 ns. Wherever possible, the relative efficiency of the forward and backward detectors was determined for *each* sample from late time data taken just above T_c, where the dynamic relaxation rate is the fastest, the decay is a pure exponential and the muons are fully depolarized quite early in the measuring window of ~ 10 μs. Under these conditions, any observed asymmetry between the forward and backward counters reflects unavoidable differences in the detector efficiencies (sensitivity, gain, energy thresholds and geometrical factors are all significant contributors), which can therefore be measured and corrected for. The time dependence of this corrected asymmetry was then fitted using a conventional non-linear least-squares minimization routine to functional forms described below.

2.1. ZF-μSR fitting functions

As a more detailed discussion of relaxation functions is given later, we restrict ourselves to a basic introduction here. The materials studied here are both structurally disordered (i.e. glassy) and magnetically disordered as a result of exchange frustration; therefore we expect a distribution of local fields. The material will contain many magnetically inequivalent interstitial sites into which a muon can localize itself. This large variety of muon sites and the effect they have on a ZF-μSR spectrum allow the magnetic field to which the muons are exposed to be described by a Gaussian distribution of local fields $\vec{B}$:

$$P_{\mathrm{G}}(B_i) = \frac{\gamma_\mu}{(2\pi)^{1/2}\Delta} \exp\left(-\frac{\gamma_\mu^2 B_i^2}{2\Delta^2}\right) \qquad i = x, y, z \tag{1}$$

where $\Delta^2/\gamma_\mu^2 = \langle B_x^2 \rangle = \langle B_y^2 \rangle = \langle B_z^2 \rangle$ and $\gamma_\mu = 2\pi \times 1.3554 \times 10^8$ rad s^{-1} T^{-1}.

For static magnetic fields about a muon, when the muon stops at $t = 0$ with its spin pointing in the z direction, the spin evolves in time as

$$\begin{aligned} \sigma_z(t) &= \frac{B_z^2}{B^2} + \frac{B_x^2 + B_y^2}{B^2} \cos(\gamma_\mu B t) \\ &= \cos^2(\theta) + \sin^2(\theta) \cos(\gamma_\mu B t) \end{aligned} \tag{2}$$

where θ is the polar angle of $\vec{B}$ with respect to the z axis.

The muon spin relaxation function for zero external longitudinal field is the statistical average of $\sigma_z(t)$:

$$G_z(t) = \iiint \sigma_z(t) P_{\mathrm{G}}(B_x) P_{\mathrm{G}}(B_y) P_{\mathrm{G}}(B_z)\, \mathrm{d}B_x\, \mathrm{d}B_y\, \mathrm{d}B_z \tag{3}$$

which yields

$$G_z^{\mathrm{KT}} = \tfrac{1}{3} + \tfrac{2}{3}(1 - \Delta^2 t^2) \exp\left(-\tfrac{1}{2}\Delta^2 t^2\right). \tag{4}$$

This is known as the Gaussian Kubo–Toyabe (KT) muon spin relaxation function, after Kubo and Toyabe who first derived this expression [19], and we follow the prescription described in [20].

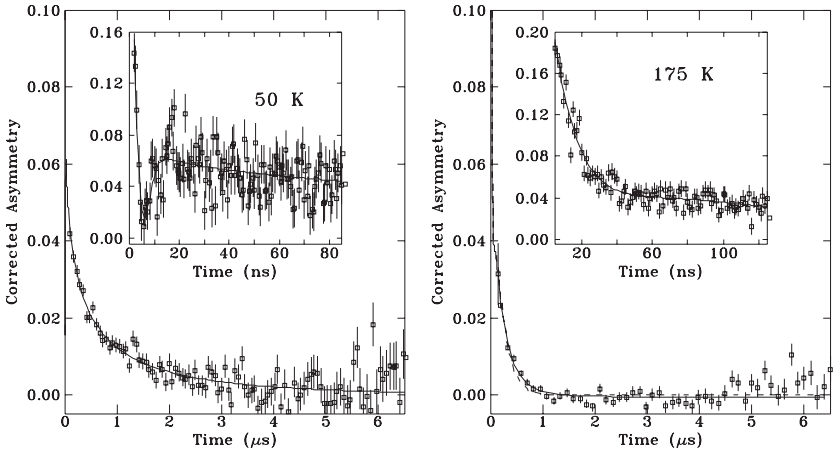

Figure 1. ZF-μSR spectra of a-$Fe_{92}Zr_8$ below T_c (left) and around T_c (right). Insets show the early time regions where the KT minimum characteristic of static order is visible. Solid curves show the lineshape calculated with the full dynamic $G_z^{KT}(t)$ (left, 50 K) and $G_z^{SG}(t)$ (right, 175 K), while dashed curves show fits using the product function $G(t)$ of equation (11).

Examining the inset to the 50 K spectrum in figure 1 we see that equation (4) correctly predicts the ZF-μSR lineshape of the static moments. The $\frac{2}{3}$ component corresponds to the muon's damped oscillations around B due to the inhomogeneity of B_x and B_y. The persisting $\frac{1}{3}$ component represents the muons that stopped where the local field axis was parallel to the initial spin direction.

In some disordered magnetic materials at any temperature (e.g. dilute alloys) and in others near a transition temperature (e.g. around T_c in spin glasses and frustrated magnets) the local static magnetic field around the muon can still be described by a Gaussian distribution. However, the sample's average field is better described by a Lorentzian distribution [21] as the moments are physically more disperse or effectively more disperse due to the substantial fluctuations.

$$P_L(B_i) = \frac{\gamma_\mu}{\pi}\frac{a}{(a^2+\gamma_\mu^2 B_i^2)} \tag{5}$$

is our Lorentzian field distribution and the probability $\rho(\Delta)$ of finding a muon site of value Δ is [21]

$$\rho(\Delta) = \sqrt{\frac{2}{\pi}}\frac{a}{\Delta^2}\exp\left(\frac{-a^2}{2\Delta^2}\right) \tag{6}$$

where $\rho(\Delta)$ was determined to satisfy

$$P_L(B_i) = \int_0^\infty P_G(B_i)\rho(\Delta)\,d\Delta \tag{7}$$

so that the total field distribution in the sample is Lorentzian (equation (5)).

To obtain the dilute alloy zero-field muon spin relaxation function, $G_z^{KT}(t)$ of equation (4) is integrated over the probability of being at a muon site with a given Δ, i.e.

$$G_z^L(t,a) = \int_0^\infty G_z^{KT}(t,\Delta)\rho(\Delta)\,d\Delta \tag{8}$$

to give the Lorentzian Kubo–Toyabe relaxation function

$$G_z^L(t) = \tfrac{1}{3} + \tfrac{2}{3}(1-at)\exp(-at) \tag{9}$$

as originally derived by Kubo [22]. Equation (9) correctly describes the static ZF-μSR signal shown in the 175 K spectrum in figure 1 and exhibits the same damped $\frac{2}{3}$ component and persisting $\frac{1}{3}$ component as are seen for the Gaussian case, but with a shallower KT minimum (figure 8; $\nu/a = 0$).

The above Gaussian KT and Lorentzian KT relaxation functions describe the lineshape due to static magnetic disorder in ZF-μSR spectra. Characterizing time-dependent disorder in ZF-μSR spectra by starting from equations (4) or (9) and including the Markovian nature of spin dynamics (strong collision model) is quite involved [20, 21]. However, the observed magnetic fluctuations are often sufficiently rapid that the motional narrowing limit of $G_z(t)$ can be applied, which takes the form of an exponential [21, 23–26]:

$$G_z^{\mathrm{D}}(t) = \exp[-(\lambda t)] \tag{10}$$

where λ is an effective $1/T_1$ muon spin–lattice relaxation rate.

Many real materials do not fall into either of these limits: the timescale of the magnetic relaxation is neither so long that the moments are effectively static, nor so short that the static contribution is washed out and only an exponential decay remains. Experimentally, the KT minimum is still observed, but the $\frac{1}{3}$ tail is no longer constant and now decays to zero. The simplest description (and one that is essentially ubiquitous in the literature; see for example [21, 23, 27–38] and references therein) of such data is provided by the following phenomenological model: it is assumed that the (effectively) static moments can be described by the above $G_z^G(t)$ or $G_z^{\mathrm{L}}(t)$ and that the time-dependent behaviour arises from a random dephasing of the muons by relatively slow (relative to the muon precession in the static field) magnetic fluctuations. This argument leads to the so-called dynamical Kubo–Toyabe relaxation (product) function:

$$\begin{aligned} G(t) &= G_{\mathrm{s}}(t) \times G_{\mathrm{d}}(t) \\ G_{\mathrm{s}}(t) &= \frac{1}{3} + \frac{2}{3}\,(1 - (\Delta t)^{\alpha}) \exp\left(-\frac{(\Delta t)^{\alpha}}{\alpha}\right) \\ G_{\mathrm{d}}(t) &= \exp[-(\lambda t)]. \end{aligned} \tag{11}$$

The KT minimum is defined by $\alpha = 1$ for a Lorentzian field distribution and $\alpha = 2$ for a Gaussian distribution in $G_{\mathrm{s}}(t)$. This product function is often sufficient for simulating the experimental data; it provides a simple picture of the system under study and is easy to compute, making least-squares fitting straightforward. For magnetic systems where there is a clear distinction between static effects in early time channels and dynamic effects in later time channels, equation (11) provides a good fit to the observed ZF-μSR pattern.

We caution that equation (11) is an *approximation* and only holds if $\Delta \gg \lambda$ [20]. This condition is not met near T_{c}, especially for highly frustrated samples, and a proper treatment of the dynamics is essential to avoid falling into the trap of using a stretched exponential in $G_{\mathrm{d}}(t)$ and variable α in $G_{\mathrm{s}}(t)$ to analyse the data. We will return to this point in more detail later.

3. ZF-μSR results

Typical μSR patterns for a-$Fe_{91.5}Zr_{8.5}$ are shown in figure 2 at 240 K (above T_{c}), 110 K (below T_{c} but above T_{xy}) and 5 K (below T_{xy}). Above T_{c} there is no static order, but magnetic fluctuations couple to the muon spin and cause an exponential decay in the observed polarization. The inset shows that the exponential continues to the earliest time measured ($\sim$1.5 ns), and no static contribution is apparent. Below T_{c}, fluctuations (e.g. magnons) continue to depolarize the muons, and an exponential decay at late times is still apparent. However, the starting point for this decay is far lower than it was above T_{c} reflecting the rapid dephasing associated with the

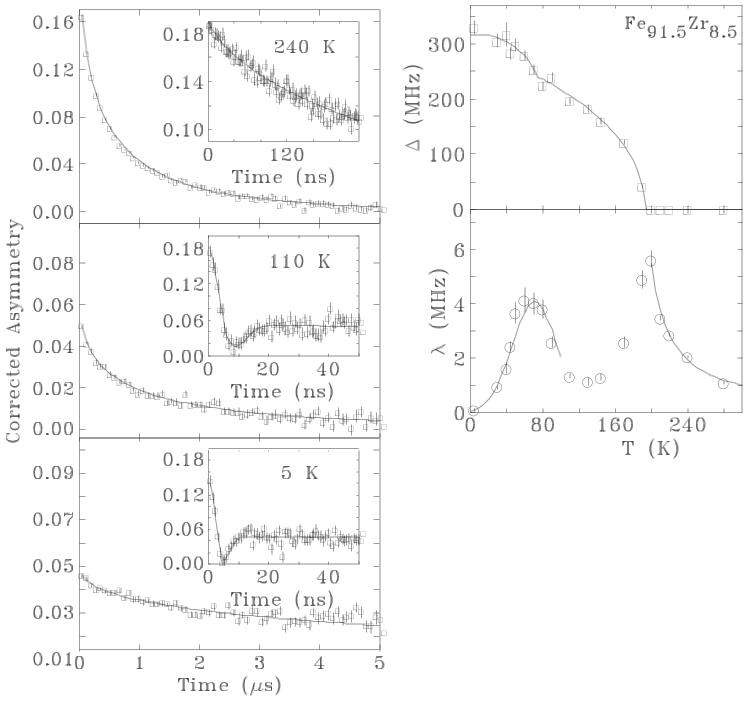

Figure 2. Left: ZF-μSR spectra of a-$Fe_{91.5}Zr_{8.5}$ above T_c (top), below T_c (centre) and below T_{xy} (bottom). Insets show the early time regions where the KT minimum characteristic of static order is visible. Note the clear separation in timescales for the static and dynamic contributions. Solid curves show the lineshape calculated with the product function $G(t)$ of equation (11). Right: temperature dependences of Δ (top) and λ (bottom) derived from product function fits (equation (11)).

precession in a distribution of static fields. The characteristic KT minimum is clearly observed at early times (inset), confirming the presence of static magnetic order. Finally, below T_{xy}, fluctuations are greatly reduced, but still present, and the KT minimum due to static order has moved to still earlier time, indicating an increase in the average field at the muon sites.

The data in figure 2 illustrate a primary strength of μSR studies: static and dynamic magnetic effects can be observed simultaneously and they are sufficiently well separated in the data that they can be distinguished with great reliability. In figure 2, the static KT contribution is confined to the first 20 ns, while the dynamic decay is spread over the remaining 5 μs. The temperatures illustrated have been chosen to be well away from the fluctuation maxima at T_c and T_{xy} so that the validity of equation (11) is not compromised, and the fits are excellent.

The right-hand panel of figure 2 shows the temperature dependences of λ and Δ derived from fits using equation (11). T_c is well defined and can be assigned to the temperature at which either λ diverges or Δ extrapolates to zero on heating. These values typically agree within the experimental error of 1–2 K. Furthermore, T_c determined by the μSR technique is in full agreement with values determined from bulk measurements (magnetization and susceptibility) and by Mössbauer spectroscopy. This agreement is observed at all compositions and levels of frustration, and serves to confirm that μSR is a consistent probe of the magnetic ordering.

On cooling below T_c, the dynamic relaxation rate falls as the fluctuations freeze out. For non-frustrated samples, this slow-down continues down to the lowest temperatures measured (typically 5 K in this work) and λ falls below 0.1 MHz [13]. For frustrated materials the decline

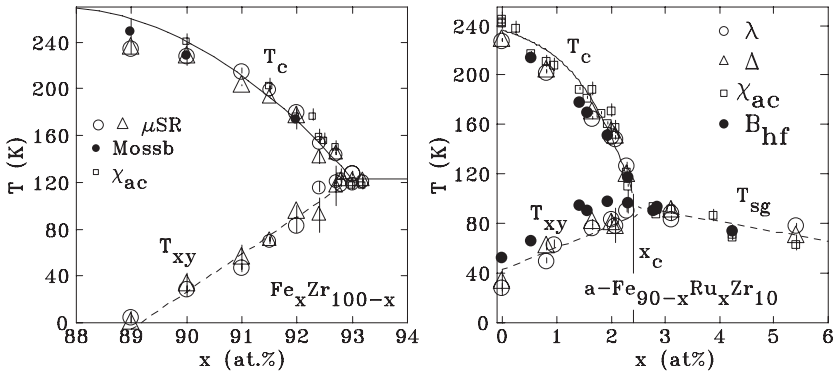

Figure 3. Left: the phase diagram for a-Fe_xZr_{100-x} showing transition temperatures derived from μSR data. Open circles show results derived from fits to the dynamic behaviour (λ) while triangles denote those from analysis of the static signal ($\triangle$). Also shown are results from χ_{ac} ($\square$) and Mössbauer spectroscopy ($\bullet$). Right: the phase diagram for a-$Fe_{90-x}Ru_xZr_{10}$ (the same symbols).

is interrupted by a second peak: T_{xy}. This peak was predicted by the numerical simulations discussed earlier [9–12]. It is clearly visible in figure 2 and provides an unambiguous signature of T_{xy}. $\Delta(T)$ also changes around T_{xy}: there is a distinct break in the temperature dependence as the transverse spin components freeze out and contribute to the static field at the muon sites. $\Delta(T)$ was fitted using the sum of two Brillouin functions (modified to allow for a distribution of exchange [39]) each with different onset temperatures and saturation values. These fits are shown as solid curves in the right-hand panel of figure 2. The break point provides a second μSR-based estimate for T_{xy}. As with the values for T_c, the two estimates for T_{xy} are generally found to be in good agreement, confirming that the static and dynamic signatures coincide as expected [9–12].

Transition temperatures for the two bond frustrated systems studied here are presented as phase diagrams in figure 3. a-Fe_xZr_{100-x} shows two transitions for $x > 89$, with T_c falling to meet an increasing T_{xy} as predicted by numerical simulations [9] and mean-field calculations [40]. The two transitions merge at a critical composition of $\sim$92.8, beyond which only a single, spin glass transition, T_{sg}, is observed. As noted earlier, there are only limited data beyond x_c as glass stability limits the accessible composition range. Both ac susceptibility (χ_{ac}) and Mössbauer spectroscopy have been used to determine T_c and these values are in complete agreement with both the dynamic and static μSR measurements.

The a-$Fe_{90-x}Ru_xZr_{10}$ system provides two advantages over the simpler a-Fe_xZr_{100-x}: (1) we have full access to the spin glass region of the phase diagram, (2) there is a clear break in the temperature dependence of the average hyperfine field ($\langle B_{hf}\rangle$) below T_c [1, 15, 16]. This break reflects the freezing of transverse spin components at T_{xy} and is directly analogous to the break in $\Delta(T)$ seen by μSR, thus providing an independent, Mössbauer-derived check of our T_{xy} assignments in this system. The results are summarized as a phase diagram in the right-hand panel of figure 3. Again, it is apparent that the static and dynamic μSR signatures of both T_c and T_{xy} are in complete agreement. Furthermore, this agreement extends to the transition temperatures derived also from χ_{ac} and Mössbauer spectroscopy. The match between the glass stability and magnetic behaviour has allowed us to extend the a-$Fe_{90-x}Ru_xZr_{10}$ phase diagram past $2x_c$, well into the spin glass region, where we observe clear evidence for a finite-temperature spin glass transition, and continued agreement between all four methods of determining T_{sg}.

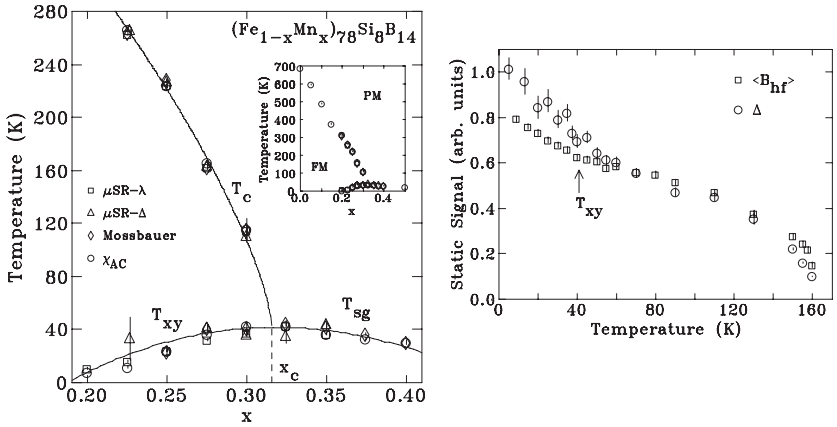

Figure 4. Left: the magnetic phase diagram for a-$(Fe_{1-x}Mn_x)_{78}Si_8B_{14}$ derived from ac susceptibility data (χ' for T_c, χ'' for T_{xy}), $\langle B_{hf}\rangle$ from Mössbauer spectroscopy and both Δ and λ from the ZF-μSR. Three transitions can be identified: ferromagnetic ordering at T_c, transverse spin freezing at T_{xy} and spin glass ordering only for $x > x_c$ at T_{sg}. Note the perfect agreement between independent determinations of T_{xy}. The inset shows data for the whole composition range studied. Right: comparison of static order signals from Mössbauer spectroscopy ($\langle B_{hf}\rangle$) and ZF-μSR (Δ) for a-$(Fe_{0.725}Mn_{0.275})_{78}Si_8B_{14}$. The data have been normalized to agree above T_{xy} in order to allow comparison of the change and signal stability below T_{xy}.

Site frustration is expected to lead to transition behaviour that is very similar to the bond frustrated case [10–12], and the phase diagram obtained for a-$(Fe_{1-x}Mn_x)_{78}Si_8B_{14}$ (figure 4) fully supports these predictions. The same decline in T_c with increasing frustration is seen; however, there is now a threshold for the appearance of T_{xy}. Unlike the bond frustrated case, transverse spin freezing in site frustrated systems does not develop until the competing sites form a percolating network [11, 12] and so ∼20% Mn is needed before T_{xy} is observed. Once both transitions are present, we again obtain perfect agreement between the static (Δ) and dynamic (λ) μSR signatures and also with bulk determinations (χ_{ac} and Mössbauer spectroscopy). The break in $\langle B_{hf}\rangle(T)$ is observed and again coincides with the break in $\Delta(T)$, but unlike in a-$Fe_{90-x}Ru_xZr_{10}$ [16], $\langle B_{hf}\rangle(T)$ and $\Delta(T)$ do not scale with each other below T_{xy}. $\Delta(T)$ rises above $\langle B_{hf}\rangle(T)$ below T_{xy} as the latter is sensitive primarily to the behaviour of the Fe moments while the former is equally sensitive to Fe and Mn moments, and it is the ordering of the AF-coupled Mn moments that dominates the changes at T_{xy} in this site frustrated system [11, 12]. The two transitions merge beyond $x_c \sim 0.31$ and the system becomes a spin glass. In principle, an antiferromagnet could emerge at high Mn dopings [11, 12], but the glass structure does not admit AF ordering and so a geometrically frustrated phase should ultimately develop.

It is clear that the ZF-μSR technique can provide a wealth of information about the ordering and magnetic transitions in frustrated magnetic materials. Its ability to unambiguously distinguish dynamic and static effects is almost unique, making it an extremely valuable probe of magnetic order. However, the dynamic and static influences on the observed muon polarization decay are not truly independent. The examples shown so far have been chosen to lie at two carefully chosen limits: almost static ($\Delta \gg \lambda$) and motionally narrowed, purely dynamic ($\lambda \gg \Delta$). Many systems present muon environments that lie outside these simple limits (this is always true around T_c, and was found to be the case over a wide temperature range in some of our more frustrated samples) and the observed muon polarization decay cannot be fitted in a meaningful way using equation (11). It is to the solution of this significant problem that we now turn.

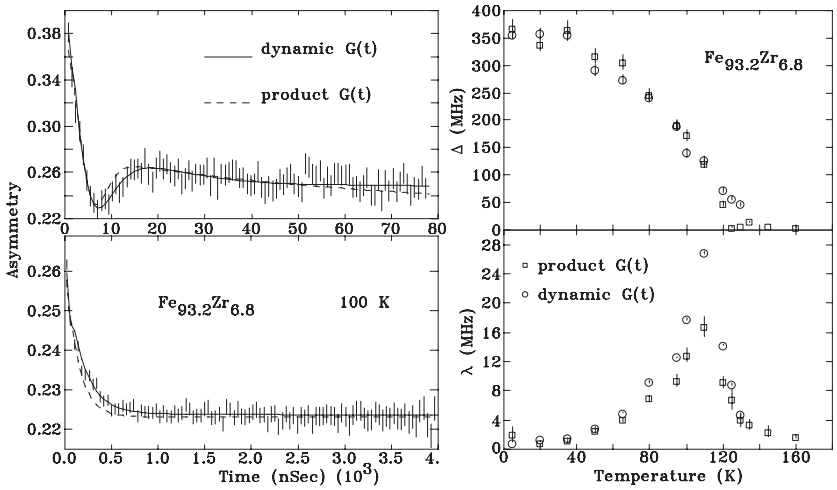

Figure 5. Left: a lineshape comparison of calculated 100 K ZF-μSR spectra of a-$Fe_{93.2}Zr_{6.8}$ using the product function (dashed curve) and dynamic KT function (solid curve). Right: fits to ZF-μSR spectra of a-$Fe_{93.2}Zr_{6.8}$ using the product function (□) and dynamic KT function (○).

4. Analysis: beyond the product function approximation

The failure of the product function as Δ approaches λ is gradual, and the distortions in the data are therefore subtle and frequently missed. The KT minimum shallows, and the simple exponential form of the long-time tail is lost. The left panel of figure 5 shows data taken at $0.8T_c$ for highly frustrated a-$Fe_{93.2}Zr_{6.8}$. The product function (dotted curve) appears to reproduce the form of the decay, but misses details around the KT minimum and the knee of the exponential has the wrong shape. The fitted value of λ/Δ is $\sim$0.2, and therefore indicates that the data set does not satisfy the requirement $\Delta \gg \lambda$. The misfit to the shape of the decay is clear. However, the full dynamic fit (described later) shows that λ/Δ is closer to 0.1, as the product function systematically overestimates Δ at the expense of λ. ZF-μSR spectra of materials where the signatures of static and dynamic magnetic effects are not clearly separated are not effectively fitted by the product function, and the derived values for Δ and λ are not correct.

Figure 6 shows a direct comparison between lineshapes from the correct dynamic Kubo–Toyabe function for a Gaussian distribution of fields, that were then fitted using the product function with $\alpha = 2$. At intermediate values of λ/Δ the product function clearly misses features in the lineshape, and cannot describe the lineshape of a ZF-μSR spectrum of a material with strong static and dynamic signals. Even at $\lambda/\Delta = 5.0$ a misfit is apparent at early times. Attempts to deal with this difficulty in the μSR literature include varying the value of α (between 1 and 2) for the static signal (this effectively makes the calculated KT minimum more shallow), and using a stretched exponential function $G_d(t) = \exp[-(\lambda t)^\beta]$ to mimic the distortions in the dynamic signal [23–25, 27, 28, 32, 36–38, 41]. This will fit the spectra; however, the product function is now being applied well outside its validity range, and the values obtained for λ and Δ are adversely affected. In addition, fits in this regime are sensitive to instrumental parameters: the initial ($t = 0$) asymmetry and the relative detector efficiencies (which gives the $t = \infty$ asymmetry). Where the static field is large, or the early time data are absent (e.g. at a pulsed source) the initial value of the asymmetry may not be properly constrained. Similarly, if the decay continues beyond the end of the time window covered, the asymptote may not be clear. Finally, even minor errors in the background corrections can

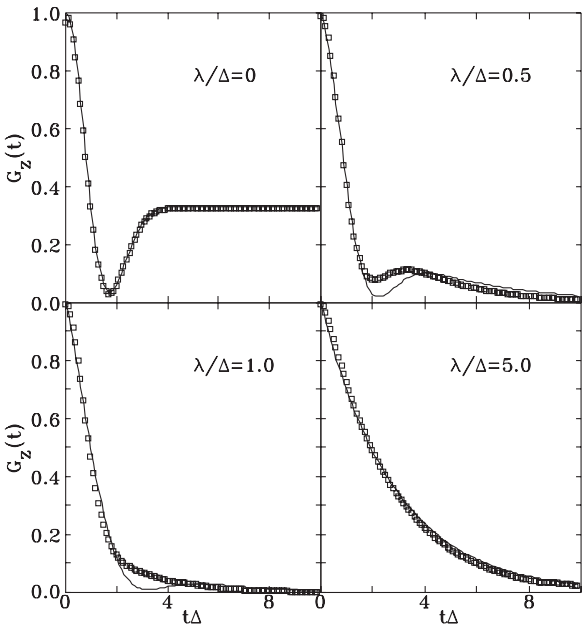

Figure 6. Zero-field longitudinal relaxation functions calculated using the dynamic Kubo–Toyabe formalism (□) and simulated with the product function, equation (11) (solid curves). Note the severe misfit for values of $\lambda/\Delta = 0.5$ and 1.0.

lead to spurious slopes at late times where the observed asymmetry is essentially zero. If a stretched exponential is used for such data, good fits with unlikely parameters are generally obtained.

The biggest drawbacks of the stretched exponential are that it is easy to code, it looks like a very wide variety of other decay forms [41, 42], it generally does a fair job of reproducing the observations and it only requires one additional fitting parameter. Stretched exponentials also yield stable, well-behaved fits even when a two-exponential fit can be shown to be more appropriate [43]. Tests of alternative forms are rare, leading to the 'conclusion' that a stretched exponential decay has been observed. However, demonstrating that the decay is in fact a stretched exponential requires that other forms be actively investigated and conclusively excluded. μSR data are rarely, if ever, adequate for this task. For a stretching parameter (β) of 0.5, one needs data with a signal (start of the exponential) to background ratio of about 100, covering about five decades of time [42]. Most data sets (including those presented here) rarely exceed a signal to background ratio of 10 and the start of the exponential is lost to the static KT signal. The data typically cover little more than two decades of time as the first $\sim$100 ns are again lost to the static KT signal. It is simply not possible to use data of this nature to establish the *presence* of a stretched exponential. By contrast, a simple log–log plot can be used to *exclude* the stretched exponential form [43].

Changes in fitted values of α and β over a temperature scan with ZF-μSR spectra of a sample will sometimes be interpreted in terms of two distinct populations of slow and fast moments in the sample, in an attempt to justify use of the product function [20, 27, 28]. However, values of α which are not 1 or 2, and $\beta \neq 1$ are more usually signs that the full dynamic Kubo–Toyabe or spin glass functions are necessary to fit the lineshape of the ZF-μSR spectrum. We shall show that using the full dynamic Kubo–Toyabe forms of the ZF-μSR fitting functions simulates experimental data where the product function fails, and provides a clear physical understanding as the physics of the model is clear and it is applicable to all measured timescales.

Several attempts have been made to develop correct solutions for the full dynamic Kubo–Toyabe relaxation function and so describe the effects of time-dependent magnetism on ZF-μSR spectra in a tractable manner. The problem is more naturally solved in Laplace space [44], displacing the core difficulty to the subsequent inversion of the Laplace transform needed to return to a solution in temporal space. A method that used a series expansion to approximate the inversion integral was developed [45], but this is limited to small static fields and rather rapid dynamics. Alternatively, iterative [46] or perturbative [47] methods may be used to solve for the relaxation function directly in temporal space, avoiding the need for taking the Laplace transform. This description has been applied successfully to systems that exhibit quite rapid dynamics in the presence of relatively small static fields [48], and while it may seem mathematically and numerically easier to implement such solutions as they remain in temporal space and avoid solving the full dynamic Kubo–Toyabe function via Laplace transform methods [20], their validity has not been fully explored. Our materials clearly exhibit very large local fields, and it is unclear how many iterations would be necessary to provide the correct convergence of $G_z(t)$ to describe the time-dependent magnetism. Additionally, the standard numerical integration methods (e.g. approximation by a sum of areas) are notoriously unstable [49–51], making non-linear least-squares fitting problematic.

The primary reason for not using the full dynamic fitting functions is that they are computationally intensive. However, increasing availability of multiple-processor clusters means that where it was once difficult to generate a single set of theoretical dynamic Kubo–Toyabe, $G_z^{\mathrm{KT}}(t)$, and spin glass, $G_z^{\mathrm{SG}}(t)$, muon spin relaxation functions [20, 21], it is now possible to least-squares fit experimental ZF-μSR spectra with the full dynamic relaxation functions. We therefore revisit $G_z^{\mathrm{KT}}(t)$ and $G_z^{\mathrm{SG}}(t)$, and make comparisons with the dynamical Kubo–Toyabe (product) function, mapping out the failure regions of the product function. By discovering the analytic solution to the Laplace transform necessary for the computation of $G_z(t)$, and by using robust numerical techniques that require typically less then ten terms for convergence, we have developed a useful method for generating the full dynamical Kubo–Toyabe lineshape. Additionally, the numerical methods used (described in detail later in the text) are based on simple recursion relations and geometrical series, so it is a straightforward matter to generate the necessary computer code. With a 6.4 gigaflop Beowulf MPI cluster, $G_z^{\mathrm{KT}}(t)$ and $G_z^{\mathrm{SG}}(t)$ were used to fit ZF-μSR spectra of a-Fe–Zr and a-Fe–Sc. Smaller fitted errors were always recorded with the full dynamic functional forms, and essentially no cross-correlations between fitted parameters were observed, leading to more stable fits. Moreover, using $G_z^{\mathrm{KT}}(t)$ and $G_z^{\mathrm{SG}}(t)$ to fit ZF-μSR spectra removes the ambiguity associated with stretched exponential product function fits. Finally, we have been able to make direct comparisons with relaxation rates determined independently using selective excitation double Mössbauer spectroscopy (SEDM), and show that they are in complete agreement [52, 53].

4.1. Dynamic lineshape calculations

The above Gaussian KT (equation (4)) and Lorentzian KT (equation (9)) relaxation functions describe the lineshape due to static magnetic disorder in ZF-μSR spectra. When the magnetic fields around the muon are time dependent, or the muon can hop from site to site resulting in a time-dependent magnetic field, the behaviour of the muon is more difficult to describe.

If a Markovian modulation of the field B occurs with a rate ν, then

$$\frac{\langle B(t)B(0)\rangle}{\langle [B(0)]^2\rangle} = \exp(-\nu t) \tag{12}$$

with the range of the field distribution $P_{\mathrm{G}}(B, \Delta)$ given by equation (1) [20, 44].

The time evolution of the muon spin relaxation function $g_z(t)$ ($\equiv G_z^{\mathrm{KT}}(t)$ of equation (4)) consists of contributions from muons which experienced no changes in the magnetic field around the muon at its site in the material up to time t, $g_z^{(0)}(t)$, only one change in the magnetic field, $g_z^{(1)}(t)$, two variations in the field, $g_z^{(2)}(t)$, and so on:

$$G_z(t) = \sum_{n=0}^{\infty} g_z^{(n)}(t). \tag{13}$$

If $\exp(-\nu t)$ is the probability that the muon did not experience a field change up to time t, with ν the relaxation time between changes, the time evolution of the relaxation function of a muon which did not experience a field change can be written as

$$g_z^{(0)}(t) = \exp(-\nu t) g_z(t) \tag{14}$$

and the time evolution of the relaxation function of a muon which underwent one field change is

$$g_z^{(1)}(t) = \nu \int_0^{\infty} \exp\{-\nu(t-t_1)\} g_z(t-t_1) \exp\{-\nu t_1\} g_z(t_1)\, \mathrm{d}t_1 \qquad (0 < t_1 < t). \tag{15}$$

In effect we have

$$G_z^{\mathrm{KT}}(t, \Delta, \nu) = \left[\exp(-\nu t) g_z(t) + \nu \int_0^t g_z(t_1) g_z(t-t_1)\, \mathrm{d}t_1 + \nu^2 \int_0^t \int_0^{t_2} g_z(t_1) g_z(t_2 - t_1)\, \mathrm{d}t_1\, \mathrm{d}t_2 + \cdots \right]. \tag{16}$$

Equation (15) can be recast in terms of a Laplace transform:

$$f_z(s) = \int_0^{\infty} g_z(t) \exp(-st)\, \mathrm{d}t. \tag{17}$$

We find [20]

$$F_z(s) = \sum_{n=0}^{\infty} \nu^n f_z^{n+1}(s+\nu) = \frac{f_z(s+\nu)}{1 - \nu f_z(s+\nu)} \tag{18}$$

and, to extract the muon spin relaxation function with time-dependent magnetic effects, the inverse Laplace transform is necessary:

$$G_z(t) = \int_0^{\infty} F_z(s) \exp(-st)\, \mathrm{d}s. \tag{19}$$

The heart of $G_z(t)$ lies in the calculation of $f_z(s)$:

$$f_z(s) = \int_0^{\infty} \{\tfrac{1}{3} + \tfrac{2}{3}(1 - \Delta^2 t^2) \exp(-\tfrac{1}{2}\Delta^2 t^2)\} \exp(-st)\, \mathrm{d}t. \tag{20}$$

The original work of Hayano *et al* [20] obtained $f_z(s)$ in two parts. The first term of $f_z(s)$ was written analytically and remaining terms were left in an integral form. Their formula (equation (20) of [20]), as published, was incorrect. This difficulty was probably due to typographical errors since numerical calculations of $G_z(t)$ presented later in the same paper have the correct form.

However, we have found that $f_z(s)$ does in fact have a full analytic form:

$$f_z(s) = \frac{1}{3}s + \frac{2}{3}\sqrt{\frac{\pi}{2}}\frac{1}{\Delta} \exp\left(\frac{s^2}{2\Delta^2}\right) \operatorname{erfc}\left(\frac{s}{\sqrt{2}\Delta}\right) - \frac{2}{3}\Delta^2 \left\{ \sqrt{\frac{\pi}{2}}\frac{1}{\Delta^3} \times \exp\left(\frac{s^2}{2\Delta^2}\right) \operatorname{erfc}\left(\frac{s}{\sqrt{2}\Delta}\right) \left[1 + \frac{s^2}{\Delta^2}\right] - \frac{s}{\Delta^4} \right\}. \tag{21}$$

$F_z(s)$ (equation (18)) and its inverse transform $G_z(t)$ need to be calculated for each time bin of a ZF-μSR spectrum. $G_z(t)$ cannot be obtained analytically. A numerical inverse Laplace transform method is necessary to determine $G_z(t)$. Many numerical inversion techniques were tested [54]; however, Weeks' method [55] using Laguerre functions was the only method robust enough to compute $G_z(t)$ over the range of times ($\sim$8 ns–10 μs) encountered in a μSR spectrum.

The basis of Weeks' methods is the expansion of an original function $f(t)$ into a series of generalized Laguerre functions:

$$f(t) \simeq t^{\alpha} \exp(-ct) \sum_{k=0}^{N} a_k \frac{k!}{(\alpha + k)!} L_k^{\alpha}(t/T) \tag{22}$$

where α, c and T are parameters. The Laguerre polynomials may be calculated from the recursion relations [54]

$$\begin{aligned} &L_0^{\alpha}(t) = 1 \\ &L_1^{\alpha}(t) = 1 + \alpha - t \\ &nL_n^{\alpha}(t) = (2n + \alpha - 1 - t)L_{n-1}^{\alpha}(t) - (n - 1 + \alpha)L_{n-2}^{\alpha}(t) \end{aligned} \tag{23}$$

and the coefficients are given by

$$\begin{aligned} a_0 &= (N+1)^{-1} \sum_{j=0}^{N} h(\theta_j) \\ a_k &= 2(N+1)^{-1} \sum_{j=0}^{N} h(\theta_j) \cos(k\theta_j) \\ \theta_j &= \left(\frac{2j+1}{N+1}\right)\frac{\pi}{2} \\ h(\theta) &= \mathrm{Re}\{((1 + \cot(\theta/2))/(2T))^{\alpha+1} F(1/(2T) + c + \imath \cot(\theta/2)/2T)\}. \end{aligned} \tag{24}$$

A final component to the solution of $G_z(t)$ is the numerical approximation of erfc(x). The complex error function is a close cousin to the complementary error function, erfc(x), via the relation

$$w(z) = \exp(-z^2)\,\mathrm{erfc}(-\imath z) = \frac{1}{\pi\imath} \int_C \frac{\exp(-t^2)\,\mathrm{d}t}{t - z} \tag{25}$$

with $z = x + \imath y$. The function $w(z)$ can be numerically approximated [56]. Since the core of $f_z(s)$ is of the form $\exp\{(\cdots)^2\}\,\mathrm{erfc}\{(\cdots)\}$, $f_z(s)$ can be recast in terms of $w(z)$. With the full analytic form of $f_z(s)$ (equation (21)) a more accurate, stable and faster numerical calculation of $G_z(t)$ is possible as $w(z)$ converges to the required accuracy with a simple four- to six-term geometric series. This avoids the necessity of integrating $f_z(s)$ in equation (20), which in terms of calculation time is much more costly as well as much less numerically stable [49–51] than the above method.

Examples of $G_z(t)$ are presented for several values of ν in figure 7. Examining the simplest case of $\nu = 0$ (i.e. the static case) given by equation (4), the $\frac{2}{3}$ component corresponds to the muon's damped oscillations around B due to the inhomogeneity of B_x and B_y. The persisting $\frac{1}{3}$ component represents the muons which stopped where the local field was parallel to the initial spin direction. For slow relaxation ($0 < \nu/\Delta < 1$), the recovery of the asymmetry to $\frac{1}{3}$ is incomplete and $G_z(t, \Delta, \nu)$ shows a decay at intermediate to late times that provides a sensitive measure of the relaxation rate, while the lineshape at early times remains essentially unaltered. For $\nu/\Delta > 1$, motional narrowing becomes significant, the static minimum is lost

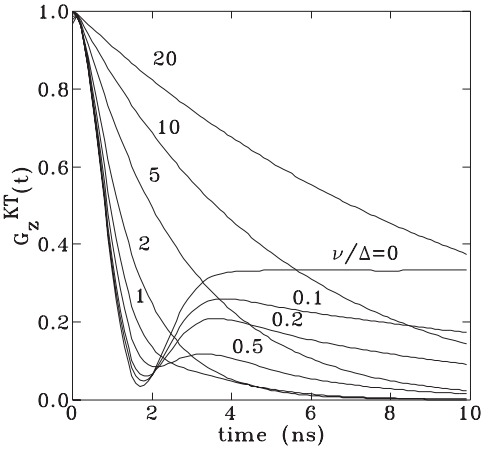

Figure 7. Zero-field longitudinal relaxation functions assuming a Gaussian distribution of fields in the sample for different relaxation rates ν.

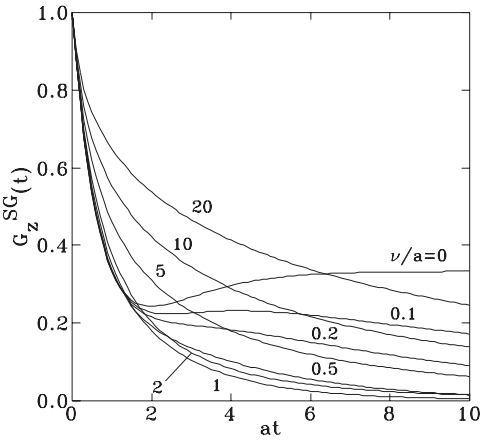

Figure 8. Zero-field longitudinal relaxation functions assuming a Lorentzian distribution of fields in the sample for different relaxation rates ν.

and the dynamic decay slows down. For fast fluctuations ($\nu/\Delta \geqslant 20$) the spin relaxation function reduces to $G_z^{\mathrm{KT}}(t) = \exp(-\lambda t)$ [21].

To obtain the zero-field muon spin relaxation function for a dilute alloy, $G_z^{\mathrm{KT}}(t)$ of equation (16) is integrated over the probability of being at a muon site with a given Δ, i.e.

$$G_z^{\mathrm{SG}}(t, a, \nu) = \int_0^\infty G_z^{\mathrm{KT}}(t, \Delta, \nu)\rho(\Delta)\,\mathrm{d}\Delta. \tag{26}$$

This is also called the spin glass (SG) muon spin relaxation function as it was originally developed to model μSR spectra of dilute alloy spin glasses [21]. Figure 8 shows some typical lineshapes for different values of relaxation rate ν. We see that for slow fluctuations ($\nu/a \simeq 1$) a decay of the persisting $\frac{1}{3}$ component occurs while the $\frac{2}{3}$ component is unchanged, although the minimum observed is distinctly shallower than that seen for $G_z(t)$ in figure 7. With faster fluctuations ($\nu/a > 2$), motional narrowing again sets in and the initial decay rate is reduced by time averaging of the fields about the muon. For fast fluctuations ($\nu/a \geqslant 20$) the spin relaxation function is approximated by a root exponential: $G_z^{\mathrm{SG}}(t) = \exp(-\sqrt{\lambda t})$ [21].

While calculations of $G_z^{\mathrm{KT}}(t, \Delta, \nu)$ and $G_z^{\mathrm{SG}}(t, a, \nu)$ are involved and require significant computational effort, advances in both computers and numerical methods have made full-solution fitting accessible and practical. Despite these advances, one still finds very few examples of the full formalism being used to fit data, and even when it used, only small-field, fast dynamics cases are treated [47, 48].

4.2. Comparison of dynamic spin relaxation functions and product function

In order to identify the region of parameter space in which the product function is valid, we have calculated curves using the full dynamic form of the dynamic Gaussian and spin glass relaxation functions developed above, and then fitted them using the product function. Parameter combinations for which the product function fails to fit the calculated curves (see for example figure 6) or where the fitted values are significantly different from those used to generate the original curves clearly indicate where the product function is an inappropriate choice. Results of this analysis are shown in figure 9, where fitted values are plotted as functions of either λ/Δ (for the Gaussian case) or λ/a (for the Lorentzian case). For Δ, λ

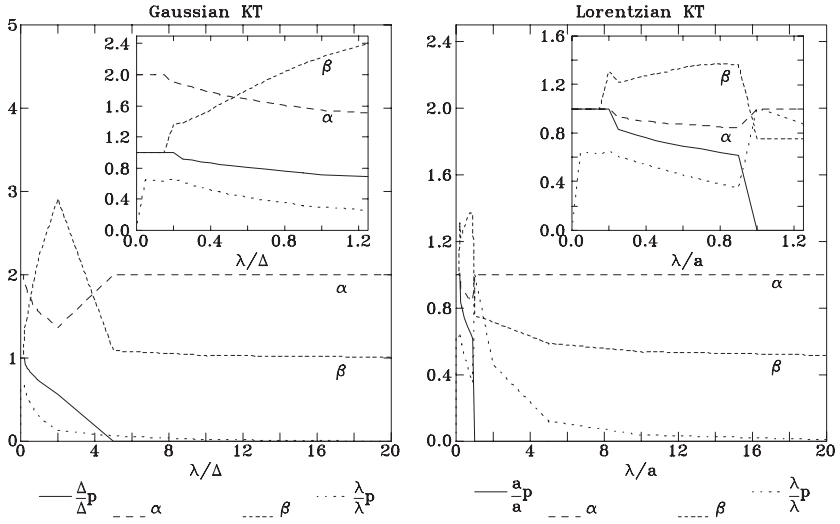

Figure 9. Left: results of product function fits to the dynamic Gaussian KT $G_z^{\mathrm{KT}}(t)$. Right: results of product function fits to the dynamic spin glass KT $G_z^{\mathrm{SG}}(t)$. $\Delta_{\mathrm{p}}/\Delta$ and $\lambda_{\mathrm{p}}/\lambda$ are the product function values versus the full spin relaxation function values.

and a, the ratio between the value returned by the product function fit (Δ_{P}, λ_{P} and a_{P}) and the corresponding value used to calculate the original curve is plotted. Departures from a ratio of one indicate that the product function is not returning the correct value.

For small values of λ/Δ ($\sim$0), when the static and dynamic μSR signals are well separated, the product function fits are quite good with α and β staying close to their nominal values of $\alpha = 1$ or 2 for Gaussian or Lorentzian static KT forms and $\beta = 1$. However, even at this limit, λ_{p} is never in good agreement with λ, showing a $\sim$30% difference.

At the other extreme ($\lambda/\Delta \gg 1$), the product function simulations appear to follow the full lineshape quite well, but $\lambda_{\mathrm{p}}/\lambda$ is severely suppressed from its ideal value of one, and the static term is essentially absent. Furthermore, the Lorentzian case yields a root exponential decay rather than a simple exponential. In this fast relaxation regime, longitudinal field μSR experiments are useful for distinguishing the static and dynamic magnetic information on a sample [27].

It is the intermediate range $0 < \lambda/\Delta < 1$ that causes the greatest problems. A KT minimum is generally apparent, but the product function gives a poor fit (see figure 6 for $\lambda/\Delta = 0.5$), and most of the fitted values are invalid. α is not severely affected for a Lorentzian field distribution, with a $\sim$20% reduction from the nominal $\alpha = 1$. However, for a Gaussian field distribution, α suffers a gradual $\sim$30% reduction in the range of $\lambda/\Delta \sim$ 0–2 followed by a gradual increase back to its nominal value of two. For both field distributions, β remains around one for $\lambda/\Delta < 0.2$. Beyond this, for a Gaussian field distribution β increases to $\sim$3, simulating some sort of power-law field distribution [41] up to around $\lambda/\Delta > 2$ where it returns to $\beta = 1$. For a Lorentzian field distribution, β increases by about 30% (suggesting a power-law field distribution) up to $\lambda/\Delta \sim 2$ where it decreases towards its root exponential limit of $\beta = 0.5$, sometimes leading to interpretation as evidence of a logarithmic decay reflecting hierarchically constrained dynamics [41]. Clearly these interpretations of β in the product function fits are unphysical, as the values obtained are numerical artifacts.

It is important to realize that in the discussion presented above, the product function was applied to *perfect* data, i.e. there are no asymmetry or detector efficiency issues, nor is there

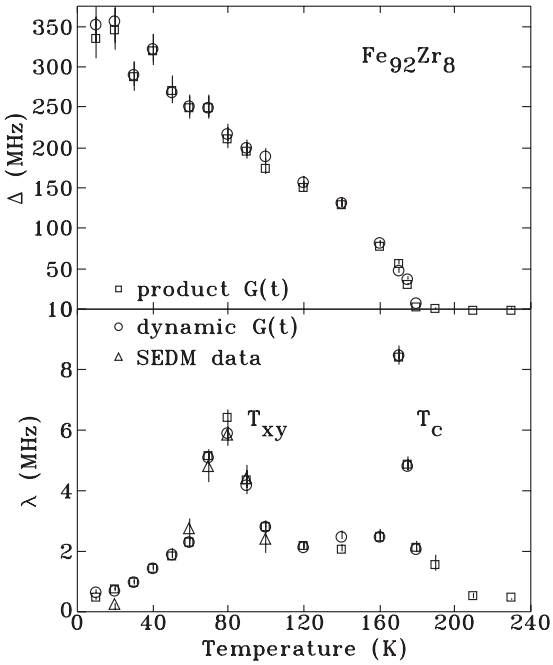

Figure 10. Fits to ZF-μSR spectra of a-$Fe_{92}Zr_8$ using the product function (□), the dynamic KT function (○) and SEDM data (△).

any statistical noise on the curves. In a real experiment, both need to be taken into account and can make fitting the experimental data more problematic.

Uncertainties in the detector efficiencies are inevitable. Ideally, both the initial asymmetry and the relative efficiency of the detectors are determined using the sample under investigation. The alternative strategy of employing a reference material fails as both parameters have a significant geometrical contribution. However, in order to use the sample being studied, it must exhibit simple behaviour at some temperature: it must fully depolarize the muons in an accessible time and the form of the decay must allow reliable extrapolation back to zero time. This latter requirement can be a serious limitation at pulsed sources where early times are not generally available. If the initial or final asymmetries are allowed to vary during the analysis, then the product function will yield greatly improved fits in the intermediate λ/Δ regime, albeit at the expense of further distorting the physically relevant parameters that are obtained from the fits.

Noise on the data is always a limiting factor, and since counting time is invariably a constraint, many of the subtle variations in lineshape that the dynamic spin relaxation functions predict will be buried in Poisson noise (compare the real data in figure 1 with the synthetic data in figure 6). This is especially relevant to the later time behaviour that the intermediate λ/Δ lineshapes exhibit, where good statistics at late times demands a large investment in collection time.

5. Results of fits with $G_z^{\mathrm{KT}}(t)$ and $G_z^{\mathrm{SG}}(t)$

First, let us examine fits to ZF-μSR data on a-$Fe_{92}Zr_8$, a frustrated magnet [13, 52], in figure 10. Fitting with the product function (equation (11), □), at T_c, $\alpha = 1$ (a Lorentzian KT) was found to describe the functional form of the spectra. Within 30 K of T_c, a Gaussian distribution of local fields, with $\alpha = 2$, described the spectra. This variation of α around T_c suggests an evolution in the local moment distribution as the collinear static order is established below T_c.

$\Delta(T)$ on cooling shows that the static magnetic field is zero until T_c is reached and collinear ferromagnetic order is established for the z component of the moments. $\Delta(T)$ steadily increases on further cooling, until T_{xy} is reached, and a more dramatic rise in the static magnetic field occurs as x and y components of the moments order with their time average no longer being zero.

The dynamic nature of the moment behaviour is revealed by $\lambda(T)$, in figure 10. When the temperature approaches the paramagnetic to ferromagnetic phase transition from above, magnetic fluctuations occur over a continuum of timescales and length scales, and ultimately diverge at T_c. Below T_c, fluctuations are much weaker, the muon depolarization is dominated by the effects of magnons and λ decreases with cooling. However, this decline is interrupted and $\lambda(T)$ increases to a second maximum at T_{xy}. The behaviour around T_{xy} is clearly non-critical as $\lambda(T)$ does not diverge. Below T_{xy} all fluctuations gradually freeze out and λ approaches zero.

Working slightly harder, $G_z^{SG}(t)$ around T_c and $G_z^{KT}(t)$ below T_c were used to fit the ZF-μSR spectra of a-$Fe_{92}Zr_8$ on a Beowulf cluster. Fit results are also shown in figure 10 (○), and we see that excellent agreement is found between the dynamic $G(t)$ and the product function $G(t)$. One advantage of the dynamic functional fit is that around T_c the spin glass function lineshape tracks the experimental data slightly better (compare the solid curve $G_z^{SG}(t)$ to the dashed curve $G(t)$ of equation (11) in the right-hand panel of figure 1). Also, the fitted errors are significantly smaller (by at least a factor of two on average) for the dynamic KT function compared to the product function, with essentially no cross-correlations (always around ∼0.1% compared with an average ∼40% cross-correlation between Δ and λ with product function fits) between fitted parameters for the dynamic KT function fits. Good agreement between product function and full dynamic spin relaxation function fits is consistent with the validity diagram of figure 9 from the fitted range of $\lambda/\Delta \sim 0.03$ describing the a-$Fe_{92}Zr_8$ data. From the spectral signal to noise ratio the fits are not sensitive to the ∼30% difference in λs between the product function and full dynamic spin relaxation function fits. Additional evidence of the fit validity is provided by selective excitation double Mössbauer (SEDM) spectroscopy results [52]. SEDM spectroscopy is a modified Mössbauer technique that can explicitly decouple static and dynamic magnetic disorder. The SEDM results indicated by the △ in figure 10 are in excellent agreement with the $G_z^{KT}(t)$ fits. Higher temperature SEDM spectra could not be collected due to an inherent shortcoming of the SEDM technique: an observable magnetic hyperfine splitting is required for the method to work. Near T_c, the six-line spectrum has collapsed to the point where the individual Mössbauer lines are no longer observable.

A 1.2 at.% increase in the iron content, and hence the level of frustration in the a-Fe–Zr system, takes us past the critical concentration of $x_c = 92.8$ [13] so the system is now in the spin glass regime. ZF-μSR data of a-$Fe_{93.2}Zr_{6.8}$ in figure 5 exhibit much the same differences between full dynamic and product function fits. However, the product function $G(t)$ of equation (11) is unable to reproduce the spectral lineshape. A stretched exponential form of $G_d(t)$ is necessary (i.e. $G_d(t) = (\exp(-\lambda t))^{\beta}$ is used in equation (11)) to describe the moment fluctuation information in the later time channels, a clear indication that the full dynamic spin relaxation lineshape needs be used to fit the spectra. This is in agreement with the validity diagram of figure 9 where the spectra fall in to the $\lambda/\Delta \sim 0.2$ range where the product function clearly fails. Notice that even with the stretched exponential product function fit, the lineshape is poorly represented (right-hand panel of figure 5) for the spectra near T_c, especially at early ($t \sim 10$ ns) and middle (70 ns $< t <$ 500 ns) time ranges.

Again, $G_z^{KT}(t)$ and $G_z^{SG}(t)$ give better fits to the data and yield smoother temperature dependences for $\Delta(T)$ and $\lambda(T)$ and reduced cross-correlations between fitted parameters. A much higher $\lambda(T)$ around T_c is fitted with the dynamic functions due to the more accurate

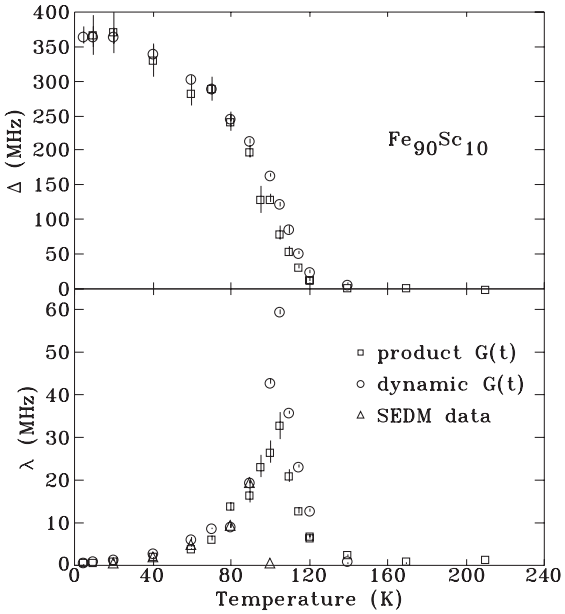

Figure 11. Fits to ZF-μSR spectra of a-$Fe_{90}Sc_{10}$ using the product function (□), the dynamic KT function (○) and SEDM data (△).

description of the ZF-μSR lineshape. While the two fitting procedures yield consistent behaviour, the product function clearly provides an inferior description of the experimental data (see for example the left-hand panel of figure 5).

a-$Fe_{90}Sc_{10}$ provides an example of a spin glass in which the fluctuations around T_c are fast enough to push the product function even further from its region of validity. Here too the static and dynamic signals in the ZF-μSR spectra can be fitted using the product function $G(t)$, shown in figure 11. On cooling through T_c, the data are best fitted using $\alpha = 1$, the Lorentzian KT functional form, while below T_c, a Gaussian distribution of local fields ($\alpha = 2$), fits the spectra. A change in the local moment distribution around T_c is thus again observed. $\Delta(T)$ is zero until spin glass order begins to establish itself, whereupon $\Delta(T)$ increases until all moments are static and in a spin glass state. Examining $\lambda(T)$, we see a steady increase in the fluctuation rate as the sample is cooled towards T_c. Once T_c is passed, moment fluctuations decrease with lowering temperature as spin glass order is established throughout the sample.

Fits with $G_z^{KT}(t)$ and $G_z^{SG}(t)$ below and above T_c, respectively, for the a-$Fe_{90}Sc_{10}$ ZF-μSR data yield similar results to the product function fits (figure 11). However, once again, fitted errors in Δ and λ are significantly smaller, and $\lambda(T)$ exhibits a much smoother transition on cooling towards T_c, with the λ s around T_c being significantly larger than those obtained from the product function. This smoother $\lambda(T)$ from $G_z^{SG}(t, a, \nu)$ fits is due to the form of the data being correctly reproduced over *all* time channels. The maximum fitted λ at T_c with $G_z^{SG}(t)$ is double that of the product function $G(t)$ with substantially smaller errors, a direct indication that the full μSR lineshape is being fitted at the transition temperature where the overall field distribution in the sample is shifting in character from Lorentzian to Gaussian. This is consistent with figure 9 for the $\lambda/\Delta \sim 0.3$–0.6 range that these spectra exhibit. Further corroboration of the $G_z^{KT}(t)$ fits is obtained by comparison with SEDM relaxation rate data for a-$Fe_{90}Sc_{10}$ below T_c [53] (△ in figure 11). Notice that the SEDM relaxation rates agree *exactly* with $G_z^{KT}(t)$ fit results at *all* temperatures up to 90 K (where $\lambda/\Delta \sim 0.1$), unlike the product function $G(t)$ fits. By 100 K, the relaxation rate is too fast for SEDM to work as the dynamic effects wash out the static contribution in the Mössbauer spectrum.

6. Conclusions

ZF-μSR is almost unique in providing local information on fluctuations in the presence of significant static magnetic order. As a result it can be used to study both the dynamic and static ordering behaviour of frustrated materials. The data presented here have shown that ZF-μSR provides detailed information that can be used to construct phase diagrams and make direct and accurate comparisons with the results of independent measurements. We have shown that partially frustrated materials exhibit two distinct ordering transitions (ferromagnetic ordering at T_c, followed by transverse spin freezing at T_{xy}) each with coupled changes in the static and dynamic behaviour. As the frustration level is increased, the two transitions merge and the system becomes a spin glass with a single transition temperature: T_{sg}.

We have shown that while a simple product function fit can provide an adequate preliminary description of ZF-μSR data, the full dynamic lineshape solution invariably yields better fits. Smaller fitted errors are obtained with essentially no cross-correlations between Δ and λ. Two possible fit parameters, α and β, are removed, greatly reducing the possible ambiguity in the fits. In addition, better agreement with other experimental probes of the dynamic magnetic behaviour in samples is achieved (e.g. compare SEDM fit results with dynamic ZF-μSR fit results). Most importantly, a consistent physical description of the magnetism in any disordered sample is possible, without resorting to the unphysical or unknown field distributions implied by $\alpha \neq 1, 2$ or $\beta \neq 1$. As Beowulf clusters like the one used to fit data here become more common, we expect the computational effort involved in fitting to the full dynamic functions to cease to be a barrier.

Product function fits allow for a good qualitative description of spectra, necessary when an experiment is under way. However, care must be exercised when comparing with results from other experimental probes sensitive to time-dependent magnetism (e.g. χ_{ac} and Mössbauer spectroscopy). Moreover, since counting time is a limited quantity, collecting spectra of sufficient quality that the full dynamic spin relaxation functions are clearly required may not be possible.

Acknowledgments

We would like to acknowledge useful discussions with M Sutton and J Gallego (McGill, Department of Physics) and M Gander (McGill, Department of Mathematics). Particular thanks are due to all those in the TRIUMF μSR group whose assistance made this work possible. This work was supported by grants from the Natural Sciences and Engineering Research Council of Canada, Fonds pour la formation de chercheurs et l'aide à la recherche, Québec, and the Australian Nuclear Science and Technology Organisation.

References

[1] Ryan D H, Tun Z and Cadogan J M 1998 *J. Magn. Magn. Mater.* **177–81** 57
[2] Lauer J and Keune W 1982 *Phys. Rev. Lett.* **48** 1850
[3] Ren H and Ryan D H 1995 *Phys. Rev.* B **51** 15885
[4] Brand R A, Lauer J and Keune W 1985 *Phys. Rev.* B **31** 1630
[5] Ren H and Ryan D H 1993 *Phys. Rev.* B **47** 7919
[6] Wiarda D and Ryan D H 1994 *J. Appl. Phys.* **76** 6377
[7] Kuprin A, Wiarda D and Ryan D H 2000 *Phys. Rev.* B **61** 1267
[8] Ryan D H, van Lierop J, Pumarol M E, Roseman M and Cadogan J M 2001 *Phys. Rev.* B **61** 140405
[9] Thomson J R, Guo H, Ryan D H, Zuckermann M J and Grant M 1992 *Phys. Rev.* B **45** 3129
[10] Nielsen M, Ryan D H, Guo H and Zuckermann M 1996 *Phys. Rev.* B **53** 343

[11] Beath A D and Ryan D H 2003 *J. Appl. Phys.* **93** 8188
[12] Beath A D and Ryan D H 2004 *Phys. Rev.* B submitted
[13] Ryan D H, Cadogan J M and van Lierop J 2000 *Phys. Rev.* B **61** 6816
[14] Ryan D H, van Lierop J, Pumarol M E, Roseman M and Cadogan J M 2001 *J. Appl. Phys.* **89** 7039
[15] Ryan D H, Cadogan J M and Tun Z 1997 *J. Appl. Phys.* **81** 4407
[16] Ryan D H, Cadogan J M and van Lierop J 2000 *Phys. Rev.* B **62** 8638
[17] Nagarajan V, Paulose P L and Vijayaraghavan R 1988 *J. Physique Coll.* **49** C8 1135
Paulose P L, Nagarajan V, Krishnan R, Voiron J, Lassri H, Nagarajan R and Vijayaraghavan R 1995 *J. Magn. Magn. Mater.* **140–44** 301
[18] Ryan D H, Beath A D, McCalla E, van Lierop J and Cadogan J M 2003 *Phys. Rev.* B **67** 104404
[19] Kubo R and Toyabe T 1967 *Magnetic Resonance and Relaxation* ed R Blinc (Amsterdam: North-Holland) p 810
[20] Hayano R S, Uemura Y J, Imazato J, Nishida N, Yamazaki T and Kubo R 1979 *Phys. Rev.* B **20** 850
[21] Uemura Y J, Yamazaki T, Harshman D R, Senba M and Ansaldo E J 1985 *Phys. Rev.* B **31** 546
[22] Kubo R 1981 *Hyperfine Interact.* **8** 731
[23] Lee S L, Kilcoyne S H and Cywinski R (ed) 1999 *Muon Science* (Philadelphia, PA: Scottish Universities Summer School in Physics) (Bristol: Institute of Physics Publishing)
[24] Dalmas de Réotier P, Yaouanc A and Gubbens P C M 1999 *Hyperfine Interact.* **120** 31
[25] Dalmas de Réotier P and Yaouanc A 1997 *J. Phys.: Condens. Matter* **9** 9113
[26] McMullen T and Zaremba E 1978 *Phys. Rev.* B **18** 3026
[27] Brewer J H 1994 *Encyclopedia of Applied Physics* vol 11 (New York: VCH) p 23
[28] Noakes D R, Brewer J H, Harshman D R, Ansaldo E J and Huang C Y 1987 *Phys. Rev.* B **35** 6597
[29] Klauß H-H, Hillberg M, Wagener W, de Melo M A C, Litterst F J, Fricke M, Hesse J and Schreier E 1997 *Hyperfine Interact.* **104** 319
[30] Bewley R I and Cywinski R 1998 *Phys. Rev.* B **58** 11554
[31] Jackson T J, Binns C, Forgan E M, Morenzoni E, Niedermayer Ch, Glückler H, Hofer A, Luetkens H, Prokscha T, Riseman T M, Schatz A, Birke M, Litterst J, Schatz G and Weber H P 2000 *J. Phys.: Condens. Matter* **12** 1399
[32] Crook M R and Cywinski R 1997 *J. Phys.: Condens. Matter* **9** 1149
[33] Lovett B W, Blundell S J, Pratt R L, Jetsädt Th, Hayes W, Tagaki S and Kurmoo M 2000 *Phys. Rev.* B **61** 12241
[34] Stewart J R and Cywinski R 1999 *Phys. Rev.* B **59** 4305
[35] Watanabe I, Akoshima M, Koike Y, Ohira S and Nagamine K 2000 *Phys. Rev.* B **62** 14524
[36] Risman T M 1990 *Proc. 5th Int. Conf. on Muon Spin Rotation, Relaxation and Resonance*; *Hyperfine Interact.* **63** 64
[37] Celio M 1986 *Proc. 4th Int. Conf. on Muon Spin Rotation, Relaxation and Resonance*; *Hyperfine Interact.* **31** 41
[38] Andreica D, Amato A, Gygax F N, Schenck A, Wiesinger G, Reichl C and Bauer E 2001 *J. Magn. Magn. Mater.* **226–230** 129
[39] Handrich K 1969 *Phys. Status Solidi* **32** K55
[40] Gabay M and Toulouse G 1981 *Phys. Rev. Lett.* **47** 201
[41] Skorobogatiy M, Guo H and Zuckermann M 1998 *J. Chem. Phys.* **109** 2528
[42] Macdonald J R 1987 *J. Appl. Phys.* **62** R51
[43] Heffner R H, Sonier J E, MacLaughlin D E, Nieuwenhuys G J, Luke G M, Uemura Y J, Ratcliff W II, Cheong S-W and Balakrishnan G 2001 *Phys. Rev.* B **63** 094408
[44] Kubo R 1954 *J. Phys. Soc. Japan* **9** 935
[45] Kehr K W, Honig G and Richter D 1978 *Z. Phys.* B **32** 49
[46] Dalmas de Réotier P and Yaouanc A 1992 *J. Phys.: Condens. Matter* **4** 4533
[47] Keren A 1994 *Phys. Rev.* B **50** 10039
[48] Dalmas de Réotier P, Yaouanc A, Heffner R H, Smith J L, Gubbens P C M and Kaiser C T 2000 *Phys. Rev.* B **61** 6377
[49] Press W H, Teukolsky S A, Vetterling W T and Flannery B P (ed) 1992 *Numerical Recipes in C—the Art of Scientific Computing* 2nd edn (New York: Cambridge University Press)
[50] Jennings W (ed) 1964 *First Course in Numerical Methods* (London: Collier-Macmillian)
[51] Carnahan B, Luther H A and Wilkes J O (ed) 1969 *Applied Numerical Methods* (New York: Wiley)
[52] van Lierop J and Ryan D H 2001 *Phys. Rev. Lett.* **86** 4390
[53] van Lierop J, Ryan D H and Cadogan J M 2002 *J. Appl. Phys.* **91** 8263
[54] Davies B and Martin B 1979 *J. Comput. Phys.* **33** 1
[55] Weeks W T 1966 *J. Assoc. Comput. Mach.* **13** 419
[56] Rybicki G B 1989 *Comput. Phys.* **3** (March/April) 85